

# The MEG Experiment – Status December 2002

A. Baldini<sup>5\*</sup>, A. de Bari<sup>6</sup>, L. M. Barkov<sup>1</sup>, C. Bemporad<sup>5</sup>, P. Cattaneo<sup>6</sup>,  
G. Cecchet<sup>6</sup>, F. Cei<sup>5</sup>, T. Doke<sup>9</sup>, J. Egger<sup>7</sup>, F. Gatti<sup>2</sup>, M. Grassi<sup>5</sup>, A. A.  
Grebenuk<sup>1</sup>, D. N. Grigoriev<sup>1</sup>, T. Haruyama<sup>3</sup>, M. Hildebrandt<sup>7</sup>, P.-R. Kettle<sup>7</sup>,  
B. Khazin<sup>1</sup>, J. Kikuchi<sup>9</sup>, Y. Kuno<sup>4</sup>, A. Maki<sup>3</sup>, Y. Makida<sup>3</sup>, T. Mashimo<sup>8</sup>,  
S. Mihara<sup>8</sup>, T. Mitsuhashi<sup>8</sup>, T. Mori<sup>8\*</sup>, D. Nicolò<sup>5</sup>, H. Nishiguchi<sup>8</sup>,  
H. Okada<sup>9</sup>, W. Ootani<sup>8</sup>, K. Ozone<sup>8</sup>, R. Pazzi<sup>5</sup>, S. Ritt<sup>7</sup>, T. Saeki<sup>8</sup>,  
R. Sawada<sup>8</sup>, F. Sergiampietri<sup>5</sup>, G. Signorelli<sup>5</sup>, V. P. Smakhtin<sup>1</sup>, S. Suzuki<sup>9</sup>,  
K. Terasawa<sup>9</sup>, A. Yamamoto<sup>3</sup>, M. Yamashita<sup>9</sup>, S. Yamashita<sup>8</sup>, J. Yashima<sup>8</sup>,  
K. Yoshimura<sup>8</sup>, T. Yoshimura<sup>9</sup>

(Collaboration for the  $\mu \rightarrow e\gamma$  Experiment at PSI)

<sup>1</sup>BINP, Novosibirsk, Russia

<sup>2</sup>University of Genova and INFN, Genova, Italy

<sup>3</sup>KEK, Tsukuba, Japan

<sup>4</sup>Osaka University, Osaka, Japan

<sup>5</sup>University of Pisa and INFN, Pisa, Italy

<sup>6</sup>Univeristy of Pavia and INFN, Pavia, Italy

<sup>7</sup>PSI, Villigen, Switzerland

<sup>8</sup>University of Tokyo, Tokyo, Japan

<sup>9</sup>Waseda University, Tokyo, Japan

December 2002

## Abstract

This status report gives an update of the ongoing activities of the  $\mu \rightarrow e\gamma$  experiment, now called MEG, as of December 2002. Results from Monte Carlo simulations, beam times at PSI and Japan, and technical developments are reported.

---

\*spokespersons

# 1 Monte Carlo simulation studies of the detector

We went on performing simulation studies of the liquid Xenon detector in order to:

- check the dependence of the energy resolution on the total number of photoelectrons (pe) collected by the photomultiplier(PMT) system;
- verify that the proposed curved shape geometry [1, 2] is the best for our experiment, by comparing the position and energy resolutions (plus obviously the acceptance and total liquid Xenon volume) with those obtainable by using a different LXe detector vessel geometry and
- provide hints for the detector optimization.

## 1.1 Energy resolution as a function of the PMTs quantum efficiency

Three different values (5%, 10% and 20%) of the PMTs quantum efficiency(Q.E.) were used in simulating the response of the liquid Xenon detector (curved shape) to 52.8 MeV photons. Photons were generated in the  $\mu$ -stopping target with an isotropic angular distribution, completely covering the fiducial inner surface of the liquid Xenon detector.

We considered two cases: an infinite and a one meter absorption length ( $\lambda_A$ ); in both cases we fixed the diffusion length ( $\lambda_R$ ) to 40 cm<sup>2</sup>.

Q.E.	5%	10%	20%
$\lambda_A = \infty$	2.0%	1.7%	1.5%
$\lambda_A = 1$ m	6%	6%	6%

Table 1: Energy resolution (FWHM) of the liquid Xenon detector for different  $\lambda_A$  and Q.E. values.

The simulation results are shown in Table 1. The photon energy was evaluated by using the total light seen by the PMTs in the  $\lambda_A = \infty$  case and by employing the “MINUIT” method described in reference [3] in the other case. As noted in reference [3], for  $\lambda_A = \infty$  the energy resolution does not depend on the method used and in any case we are interested here only to the relative differences among the three different Q.E. hypotheses.

From the results presented in Table 1 we can conclude that:

- in the  $\lambda_A = \infty$  case there is a dependence of the energy resolution on the total pe number. The resolution should increase of a factor two between the 5% and 20% cases were it dominated by pe statistics. Since this is not the case, other effects, such as back scattering of low energy photons off the calorimeter entrance wall or shower losses near its sides, contribute to the energy resolution too.

---

<sup>2</sup>The diffusion length is the one mainly determined by the Rayleigh scattering (no photon disappearance), while the absorption length is the one associated with the photon disappearance.

- in the  $\lambda_A = 1$  m case the resolution is dominated by the convolution of the calorimeter non-uniformity, due to the finite absorption length, and the shower fluctuations.

Since the absorption length in the experiment could be larger than one meter it could be important to try and improve the performance of the PMTs. We are also performing the simulations shown above with intermediate ( $2 \div 5$  m ) absorption lengths.

## 1.2 Comparison with the resolutions obtainable in a box-type detector

We evaluated the energy and position resolutions obtainable for 52.8 MeV photons in a box-type detector ( $100 \times 50 \times 50$  cm<sup>3</sup>) called VLP (Very Large Prototype) already described in reference [3]. We fixed  $\lambda_A = 1$  m and  $\lambda_R = 40$  cm.

For position resolution studies we isotropically generated 52.8 photons from a target at 65 cm from the VLP, entering the detector through one of its largest surfaces, in a  $40 \times 20$  cm<sup>2</sup> fiducial window, in order to avoid lateral shower losses.

Photon position is determined by means of a weighted average method (see [3]). Since the photon incidence direction is in general not orthogonal

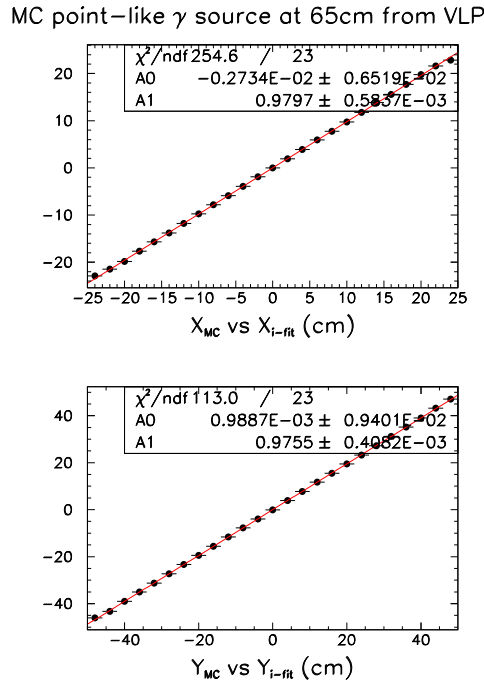


Figure 1: Correlation between the reconstructed and generated photon positions in the VLP detector. A  $\approx 3\%$  correction is needed on both  $x$  and  $y$  coordinates.

to the detector, a bias in the position measurement is present (see Figure 1) and must be corrected by using the knowledge of the photon conversion point given by the Monte Carlo simulation.

After this correction (which could represent a systematic error source, practically absent in the curved calorimeter case) we end-up with a position resolution which is equal to that obtained with the curved detector: 10.6 mm (FWHM).

For energy resolution comparisons we used the “linear fit method” described in [1, 2] to reconstruct photon energies. We computed the energy resolutions of photons hitting the two detectors (the VLP and the curved one) in a  $5 \times 5 \text{ cm}^2$  window at the center and at 12 cm from the center (see Figure 2). The energy resolution of the curved detector is only slightly worse than that of the VLP ( $4 \div 4.1\%$  against  $3.5 \div 3.6\%$ ). We conclude that the proposed (curved) geometry

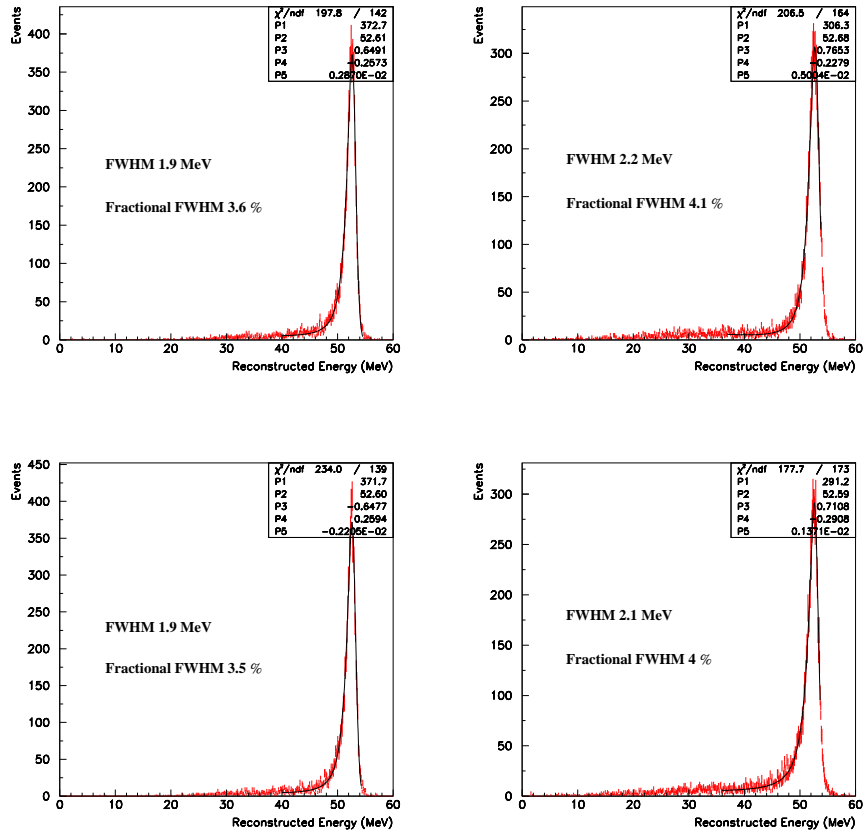


Figure 2: Comparison between the energy resolutions obtained by using the “linear fit method” in the VLP (left plots) and in the curved detector (right plots). Top: results in a  $5 \times 5 \text{ cm}^2$  window around the detector center. Bottom: the same in a  $5 \times 5 \text{ cm}^2$  window centered at 12 cm from the detector center.

seems to be well chosen since, comparing to the box-type detector, one pays

with a slightly worse energy resolution ( $10 \div 15\%$ ) a higher angular acceptance, a much lower liquid Xenon volume and no position resolution “bias”. Even in this case we plan to perform the simulations shown for other absorption length values.

### 1.3 Effect of segmentation on the energy resolution and photon detection efficiency

We studied also the effect of segmentation. This study was done by using the Tokyo Monte Carlo simulation code with a different algorithm to reconstruct the photon energy from that employed in the above studies. Therefore the results should be used, at the moment, only for comparing segmented and non-segmented geometries.

In this study as a very simple geometry, 3 walls are inserted in the detector at the angles of  $-60^\circ$ ,  $0^\circ$ , and  $60^\circ$  in  $\phi$  direction with a thickness of 80mm each (the minimum thickness to support two layers of the PMT). In these volumes PMTs and holders are placed. Scintillation light which reaches either face of these walls covered by PMTs with a maximum density is counted using the same algorithm for the other walls. In this study the Q.E. of the PMT is supposed to be 15% and all walls are covered by the PMTs most densely (50% coverage). Events are simulated for non-segmented and segmented geometries with  $\lambda_A = 5\text{m}$  and  $\infty$ , and  $\lambda_R = 40\text{cm}$ . 52.8 MeV photons are generated randomly in the acceptance of the detector. The obtained energy spectra are shown in Figure 3. It can be seen that, due to the insensitive volume occupied by the PMTs and holders, event detection efficiency is lost compared to the non-segmented geometry. The resolutions and relative loss rate of the detection efficiencies are summarized in Table 2. Here the detection efficiency is estimated by counting the number of events in the range of  $0.99 \leq E_\gamma/52.8\text{MeV} \leq 1.01$ .

	non-segmented (FWHM)	segmented (FWHM)	Efficiency loss (relative)
$\lambda_A = 5\text{m}$	3.7%	3.7%	28%
$\lambda_A = \infty$	1.5%	2.0%	44%

Table 2: Comparison of the energy resolutions for non-segmented and segmented geometries. Relative loss of efficiency is also quoted.

For an absorption length longer than 5 m it is clear that segmenting the detector will not improve its performance at all. The only effect is a loss of the detection efficiency. On the other hand in the case of absorption length shorter than 5m, there would be a possibility to achieve better sensitivity of the experiment by optimizing the acceptance and loss of detection efficiency. Further detailed study is needed to clarify the case.

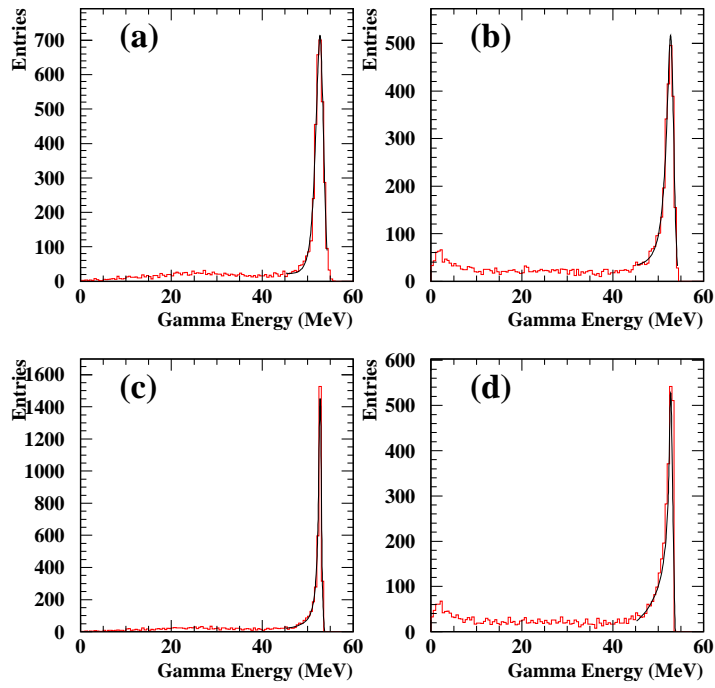


Figure 3: Energy spectra for 52.8 MeV photons with non-segmented and segmented geometries. (a) for  $\lambda_A=5\text{m}$  non-segmented, (b) for  $\lambda_A=5\text{m}$  segmented, (c) for  $\lambda_A=\infty$  non-segmented, and (d) for  $\lambda_A=\infty$  segmented.

## 2 $\pi$ E5 Beam Studies:

Results obtained from an initial beam study in the  $\pi$ E5 "U"-branch, in October 2001 [4] showed that producing a stopped surface muon beam, with sufficient intensity and free from beam correlated positrons could not be achieved using a degrader for simultaneous particle separation and momentum degradation, owing to the limitation in vertical phase space acceptance of the last two beam elements in the "U"-channel.

The goal for 2002 was, not only to find a viable alternative method but also to obtain the data necessary to make a choice of branches ("U" or "Z") for the future experiment. In July/August 2002, an alternative approach was used in the "U"-channel of  $\pi$ E5, employing separated stages of particle separation and momentum reduction. Provisional results showed that not only could a suitable beam be achieved using this method but that this method should also be employed in a comparative study of the "Z"-branch, so enabling a decision to be made, as to which branch to use for the experiment early in 2003.

This comparative study was started in November 2002 and currently underway, with promising results to date. The "Z"-branch, previously used for the  $\mu \rightarrow e$  conversion experiment, SINDRUM 2, extracted the beam, using a large 8.5 m long superconducting solenoid (PMC) which could be moved into the shielding to connect to the last bending magnet ASC, via a rail system c.f. Figure 4.

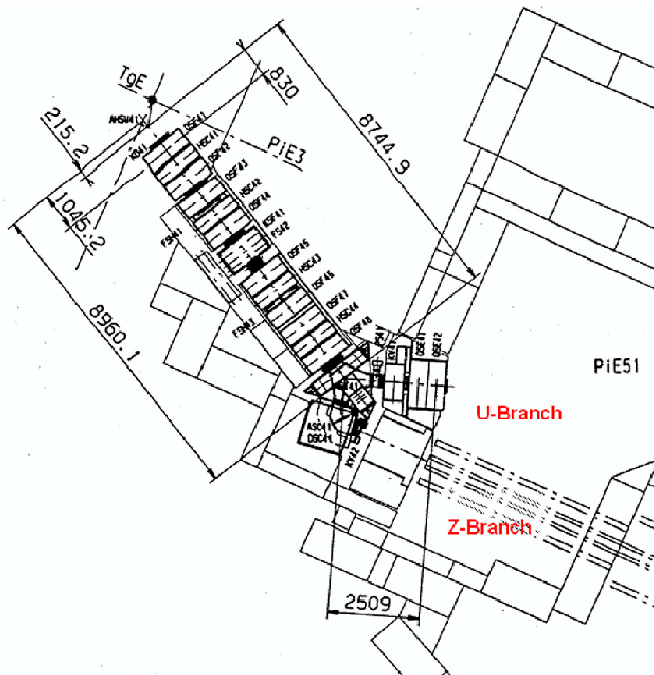


Figure 4:  $\pi$ E5 Beam line and its two branches, the so-called "U" and "Z" channels.

As the PMC is not suitable for the MEG-experiment for optical reasons, a

new extraction method was necessary to couple to the bending magnet, some two metres inside the shielding. A solution, employing a quadrupole triplet, was initiated soon after the end of the August run and involved the construction of a completely new system of newly delivered quadrupole magnets as well as a shielding wagon. Owing to the efficient cooperation and flexibility shown by many of the infrastructure groups involved in the realization, it was possible to install the triplet during a two-day shutdown at the end of November, thus enabling the planned beam time to be utilized with only a short delay.

The results presented below are based predominantly on an on-line analysis, this due to the short time period between the two beam periods and also the preparations required.

## 2.1 "U"-branch Measurements

The measurements undertaken in the July/August run, aimed to simulate the entire beam line layout for the MEG experiment, apart from that of the COBRA magnet [5]. A schematic of the layout, as well as the tools involved in the measurements of the beam phase space and rate measurements, are shown in Figure 5, for the last measurement in the "U"-branch. The principle is applicable to all setups.

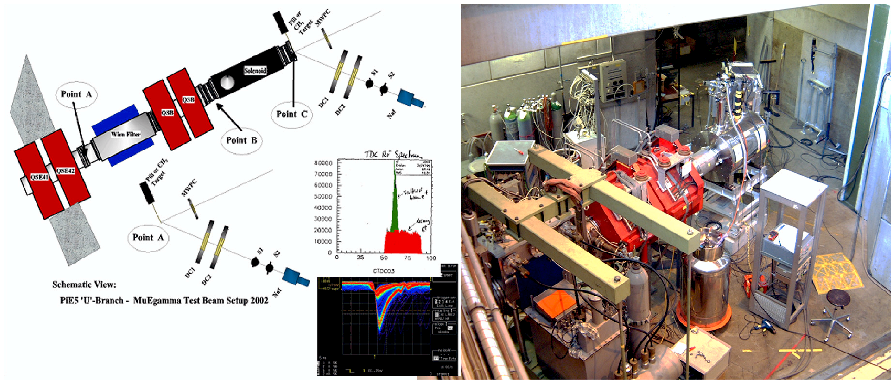


Figure 5: "U"-branch area layout, schematic and photograph, showing the the measuring locations: Point A, post QSE41/42 doublet, point B after the separator and the final location, point C, post solenoid. A 4-micron thick differential pressure window, made of Mylar, was placed just after QSE42 in order to suppress rest-gas activation for the measurements. Also shown are the detector systems used, a small "pill" scintillation counter, mounted on an X-Y scanner. A scintillation counter telescope S1,S2, together with a large NaI(Tl)-counter. A set of fast multi-wire proportional chambers (MWPC1/2), used for tracking, and a profile MWPC.

Measurements were taken at three locations in the area, corresponding to the three separate measurement phases, each series performed after optimization of the beam at the respective point, namely, Phase A, at the entrance, immediately downstream of the QSE42 quadrupole magnet, Phase B, after the separator, both with and without a suitable collimator system in front of the solenoid,

and finally Phase C, post solenoid, using both a thick and a thinner target, equivalent to that of the proposal [5][1].

The phase A measurements included, apart from the phase-space determination (spot-sizes, divergences) and the surface muon and beam positron rates, also the measurement of the muon momentum spectrum, ranging from 25-32 MeV/c, including the kinematic edge of pion decay, so enabling a check of the momentum calibration of the beam and momentum byte. The beam rate-dependence on various slit settings was also studied. Finally, a consistency check of measurement techniques was performed, using a well-collimated beam and four separate counter systems: two 2 mm thick scintillator pills of 1 and 2 mm diameter respectively, an integral counter of the same thickness but large enough to contain the whole beam spot and finally the NaI-counter and telescope system. A rough analysis showed that the four methods gave consistent results of the rate of muons to within about 20%.

Figure 6, shows an example of a two-dimensionally scanned muon beam spot, at point A.

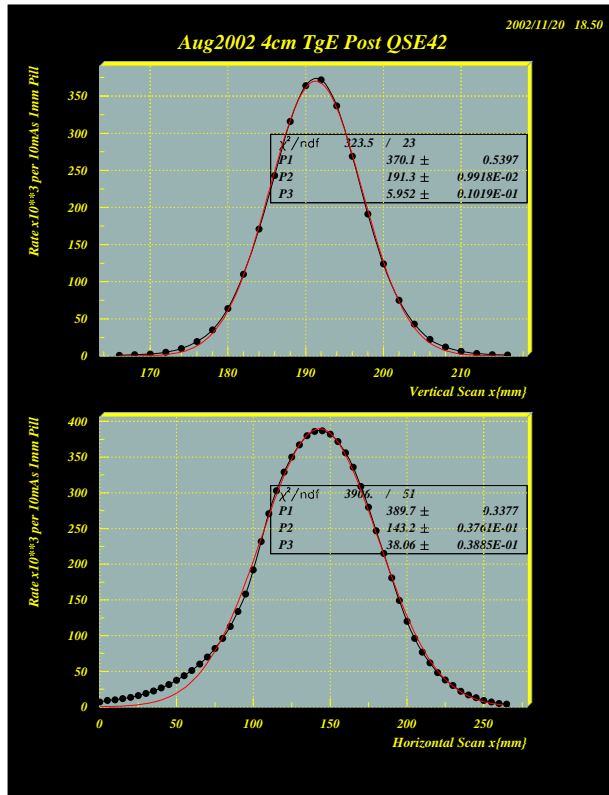


Figure 6: Vertical and horizontal beam spots measured at point A, for a 4 cm thick target E, by scanning with a 2 mm diameter pill scintillator. A gaussian fit is also shown in the figure.

Integration using two independent methods give a consistent total of:

$$N_{\mu^+} \sim 1.3 \cdot 10^8 \mu^+ s^{-1} \quad (1)$$

at  $1800\mu\text{A}$ , for a 4 cm thick Target E, which has been measured to give a factor of 1.8 times less surface muons than the 6 cm thick target specified in the proposal [5]. An independent measurement was also made to check that the phase space ellipse was not tilted with respect to the scanned axes. Phase B rate measurements, were also supplemented with beam spot scans at four different positions after the separator, in order to obtain an accurate determination of the divergencies, necessary for the design of the future beam transport solenoid. The Wien filter was run at a maximum voltage of 175 KV, even though the electrodes are 19 cm apart (largest available gap at PSI), compared with the beam pipe of 32 cm. This causes a loss in transmission, initial estimates of the transmission with respect to the rates at point A, give  $\leq 60\%$ . The separation between muons and beam positrons at this setting is shown in Figure 7 with a separation close to 11 sigma, amounting to a 24 cm vertical separation physically.

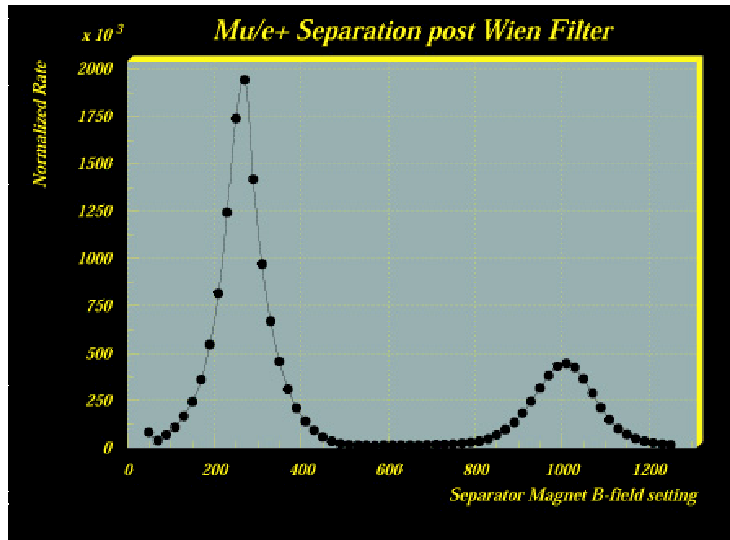


Figure 7: Separation Quality, measured at a separator voltage of 175 KV, using a 2 mm diameter pill scintillator placed after the Wien filter. The two visible peaks seen when the separator magnetic field is scanned and the rate measured by the pill scintillator at minimum threshold are due to beam positrons (270) and surface muons (1010). The physical vertical separation of almost 11 sigma amounts to about 24 cm spatially.

During Phase C, measurements were made after the superconducting solenoid, i.e. point C. Although not ideal from the aperture point of view (20 cm), this solenoid was partially meant to test the principle of momentum reduction by means of a degrader placed at an intermediate focus in the solenoid. Not only were a full set of phase space measurements taken and rates determined, but also a study of the separation quality was made. A range curve was measured using polyethylene foils ranging from 190 microns to about 1600 microns. A series of measurements were also taken using various sizes of target with the scintillator telescope, NaI-counter and tracking chambers. These data, together with the ones from the present run will be analyzed starting in January.

Figure 8 shows the final spot-size achieved at the stopping target, post

solenoid. The widths in sigma for the vertical and horizontal profiles, respectively 6.5 mm and 5.5 mm closely match those values specified in the proposal [5].

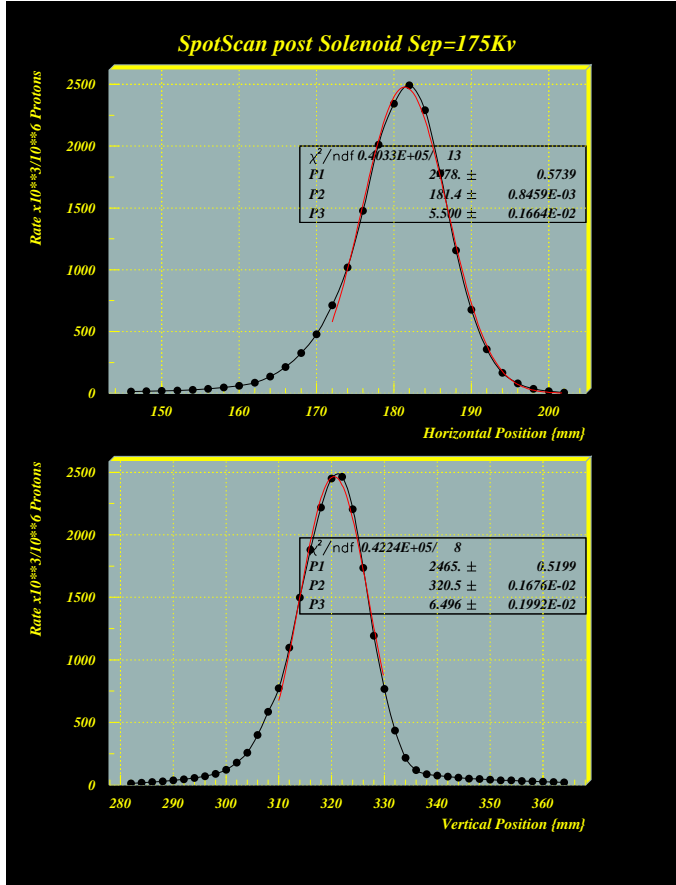


Figure 8: Beam Profiles for muons, rate versus x- and y-positions, as measured, using the pill counter at the final stopping target position after the superconducting solenoid. The values of the widths, given in sigmas by the parameter P3 of the corresponding gaussian fits closely match the proposal values of 5 mm.

## 2.2 Comparative Results in the "Z"-branch

In order to extract the beam from the "Z"-branch a quadrupole triplet was used to couple to the last bending magnet ASC. As previously mentioned this together with a newly constructed wagon, was used to insert the magnets approximately 2 m into the shielding. The insertion took place during a 2-day shutdown period of the accelerator in November of this year. Figure 9 shows the placing of the newly constructed triplet onto the wagon, which was subsequently used to insert it.

Very preliminary results show that based on similar measurements to those described above, for phases A and B of the "U"-branch, a comparative number of muons could also be transferred into the area. The measured transmission



Figure 9: Photograph shows the triplet consisting of QSM-quadrupole magnets being lowered onto the the wagon designed to insert the elements into the "Z"-branch of the  $\pi$ E5 beamline.

factor through the Wien filter, using two triplets, c.f. Figure 10, was found to be of the order of 67% i.e. significantly better than that using two doublet combinations. However, the separation quality seems somewhat worse, though still very good. The goal for the November/December run period was to obtain the comparative data for phases A and B in the "Z"-branch, thus enabling the choice of area to be made for the final experiment, as well as allowing the design of the beam transport solenoid to continue in parallel until the phase C measurements can be completed after the accelerator shutdown.

### 2.3 Tentative Conclusions

Intensive beam studies during the course of the year 2002 have shown that a suitable, intense beam of surface muons can be produced, using a Wien filter for particle separation and a solenoid and target system to produce a small beam spot with dimensions comparable to those outlined in the proposal. However, a careful offline analysis of the collected data is still required in order to study the separation quality in detail, although from initial figures obtained, the background seems to be at the per mille level.

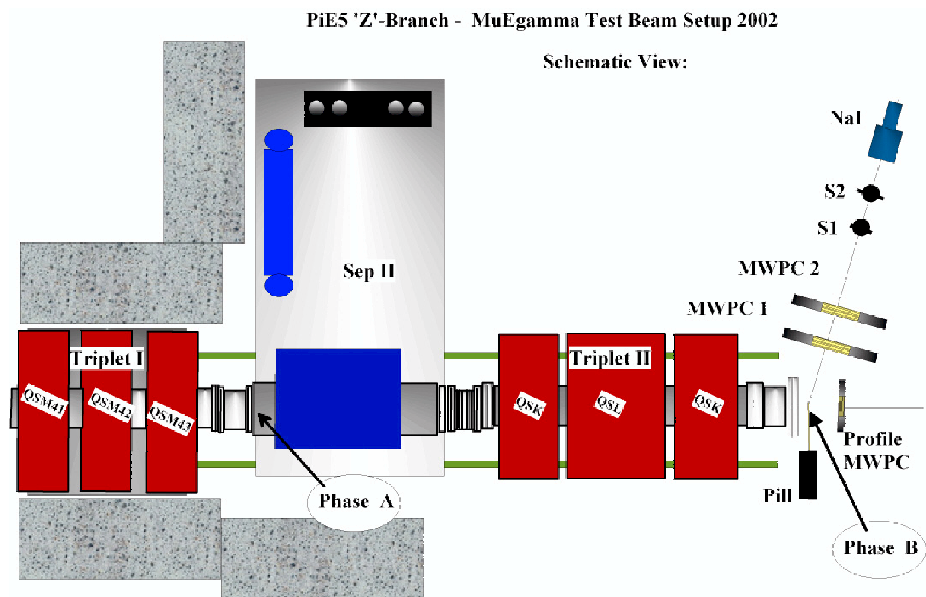


Figure 10: Schematic showing the layout of the measurements undertaken in the "Z"-branch of the  $\pi E5$  beamline, during November and December 2002.

### 3 COBRA magnet

As described in the last progress report[1], the construction of the COBRA magnet was started. The construction of a central part of the magnet which consists of the central coil, two gradient coils and an aluminum support structure was already finished and an excitation test of the central part was separately performed. In this section the current status of the construction of the magnet will be described concentrating on the the excitation test of the central part of the magnet.

#### 3.1 Excitation test of the central part of the magnet

After the cable winding of the central coil and gradient coils, they were assembled together with an aluminum support structure as shown in Fig. 11. Because the current density and magnetic field are maximized and an axial component of the electromagnetic force concentrates in this part of the magnet, it was carefully designed from mechanical and superconducting viewpoints. The excitation test of this part was separately performed prior to an assembly of all the coils in order to measure various properties of the magnet such as temperature distribution, quench propagation and mechanical strength. Analysis of the data from the excitation test is in progress and the results will be reported in detail in a separate report.



Figure 11: The central part of the COBRA magnet which contains the central coil, two gradient coils, and an aluminum support structure.

A setup of the excitation test is shown in Fig. 12. The magnet was installed inside a vacuum cryostat and thermally connected to a liquid helium tank. Properties of the magnet can be studied under the similar thermal condition to

that of the final magnet where the coils will be cooled in a vacuum cryostat by using mechanical refrigerators.

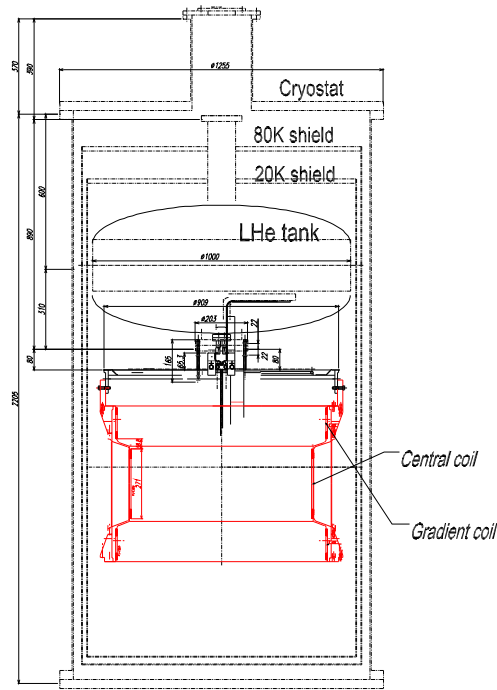


Figure 12: The setup of the excitation test of the central part of the COBRA magnet.

Temperature sensors (Pt, CGR, PtCo), strain gauges and SQDs(Superconducting Quench Detectors) were attached to the coils and support structure in order to measure the temperature distribution, strength of the magnet and quench propagation in the magnet.

Fig. 13 shows the temperature change measured at various points in the magnet during a precooling prior to the excitation test. The magnet was slowly cooled down to minimize a stress caused by a temperature difference in the magnet. Maximum temperature difference during the precooling for 55 hours was around 30 K as shown in Fig. 13.

The conditions of the excitation of the magnet are listed in Table 3. Thirteen sets of the excitation of the magnet with various coil current were performed. Since the two end coils were not available in this test, we had to excite the magnet with a higher coil current than that in the final magnet in order to simulate the same superconducting and mechanical load as in the final magnet. There are some target values concerning the coil current. At a coil current of 375 A a load line ratio of the superconducting cable in the central coil reaches the same value as that in the final magnet. At a coil current of 445 A a shearing stress between the central coil and support cylinder exceeds a maximum allowed shearing stress defined as  $1/4 \times \sigma_{\text{breakdown}}$  where  $\sigma_{\text{breakdown}}$  is a breakdown stress for the gluing between the coil and support cylinder. The breakdown stress

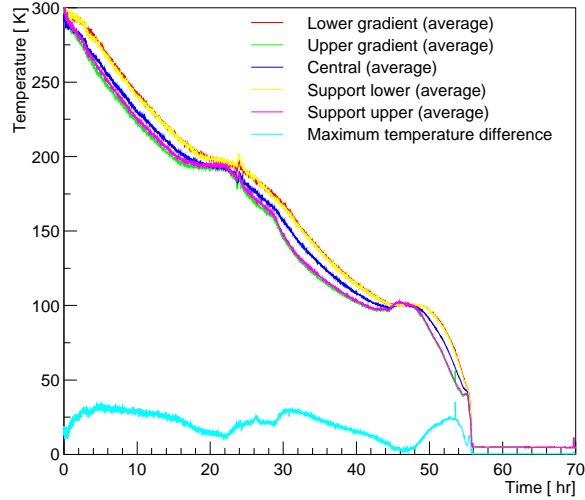


Figure 13: The temperature change measured at various points in the magnet during a precooling for 55 hours.

had been measured to be 7.8 MPa in the previous test[6]. At a coil current of 463 A a hoop stress in the support cylinder exceeds a maximum allowed stress for the aluminum (A5083) at 4 K. At a coil current of 486 A the same axial force as that in the final magnet acts on the support cylinder.

Although the analysis of the data is still in progress, some results are briefly shown here.

In the excitation #4, the magnet was excited with a coil current of 360 A which is the same coil current as that in the final COBRA magnet. Fig. 14 shows the coil current and temperature of the coil and support structure as a function of time in the excitation #4. Magnetic field at the center of the magnet was measured to be 0.94 T for 360 A coil current as expected.

At the end of this excitation, the coil current was intentionally cut off. The coil current was decayed with a time constant determined by an inductance of the magnet and protection resistor. A quench occurred due to a Joule's heat by a current induced by  $d\Phi/dt$  when the coil current was decayed down to 257 A.

Fig 15 shows the measured voltage across voltage taps in the central coil and gradient coils which will be used to sense a start of the quench in an operation of the final magnet. We can see a voltage appears first in the lower gradient coil and then in the other coils. It indicates the quench occurred first in the lower gradient coil and it propagated all over the magnet. Fig. 16 shows the temperature change of the coils and support structure when the quench occurred. In this quench the temperature of the upper gradient, central and lower gradient coil rose up to 46, 44 and 102 K, respectively.

In the excitation #11, a heater quench test was performed with a coil current of 360 A. A quench was provoked by using small heaters attached to the coils.

Table 3: The experiment profile of the excitation test.

Excitation	Coil current[A]	Test
#1	50	Excitation and current switch-off
#2	100	Excitation and current switch-off
#3	200	Excitation and current switch-off
#4	360	Excitation and current switch-off
#5	200	Heater quench at single coil
#6	200	Heater quench at three coils
#7	300	Heater quench at single coil
#8	300	Heater quench at three coils
#9	400	Excitation
#10	463	Excitation
#11	360	Heater quench at three coils
#12	486	Excitation
#13	400	Excitation

A pulse with  $10.8\text{ W} \times 300\text{ msec}$  was simultaneously put into all the heaters to provoke the quench in all the coils. It is important to avoid a local quench in a single coil and dissipate the stored energy all over the magnet in order to protect the magnet in the event of quench.

Fig. 17 shows the temperature change of the coils and support structure when the quench occurred. In this quench the temperature of the upper gradient, central and lower gradient coil rose up to 55, 79 and 123 K, respectively.

Strains of the coils and support structure were measured during the excitation test with strain gauges in order to measure the mechanical strength of the magnet. Both of  $z$ - and  $\theta$ - components were measured. Fig. 18 shows change of the strains in the excitation #12 as a function of square of the coil current which is proportional to the electromagnetic force acting on the magnet. In this excitation the coil current was raised up to 486 A which is the maximum coil current in the series of excitations and will produce the same axial force acting on the support cylinder as that in the final magnet. This figure shows a good linear relation between the strain and square of the coil current (electromagnetic force) although slight hysteresis can be seen in some strain gauges. It indicates that the mechanical support structure of the central part of the magnet work well for the expected axial force in the final magnet.

In summary, we performed the excitation test of the central part of the COBRA magnet to measure the superconducting and mechanical performance of the magnet. The magnet was excited with a coil current up to 486 A and tests of the cutoff of the coil current and heater quench were also performed. The quench propagation and mechanical strength were measured with temperature sensors, strain gauges and SQDs. Although the detailed analysis is still in progress, no major problem was found concerning the mechanical strength and superconducting performance of the magnet.

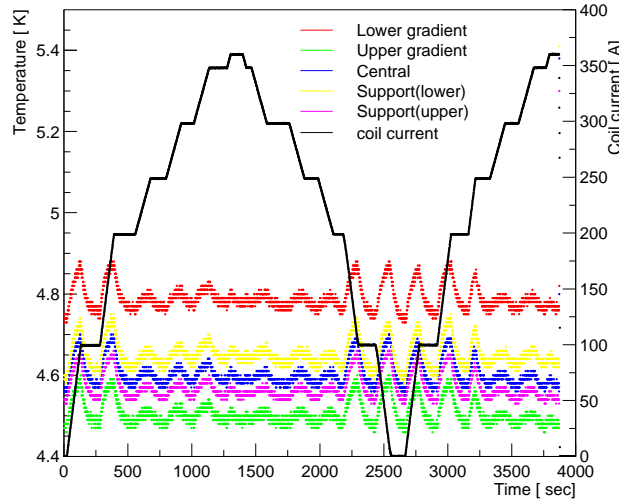


Figure 14: The coil current and temperature of the coil and support structure as a function of time in the excitation #4.

### 3.2 Construction schedule

The cable winding of the end coils is ongoing (Fig. 19). Since a block winding technique is employed in the end coil as shown in Fig. 19, the winding is carefully progressed. The winding of one end coil was completed. It is being assembled with a support cylinder. After the winding of the end coil, the two end coils will be assembled with the central part of the magnet. The construction of the cryostat, power supply and control system are also starting. All the coils will be installed into the cryostat in January next year. In next February the construction of the magnet will be finished and the total test will be performed. After that the magnet will be shipped to the PSI.

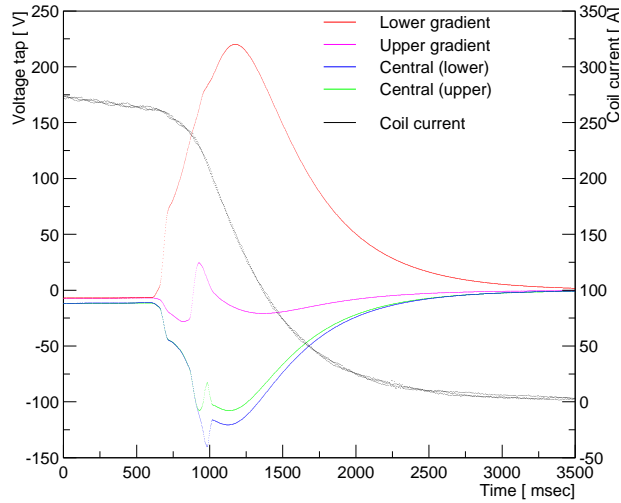


Figure 15: The measured voltage across the voltage taps in the excitation #4.

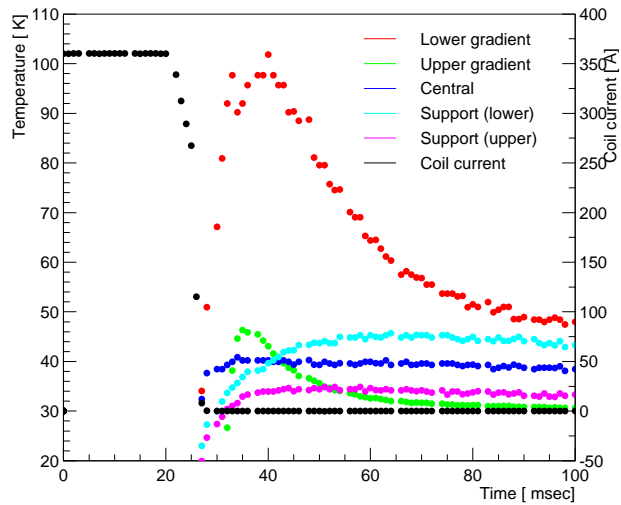


Figure 16: The temperature change of the coils and support structure when the quench occurred in the excitation #4.

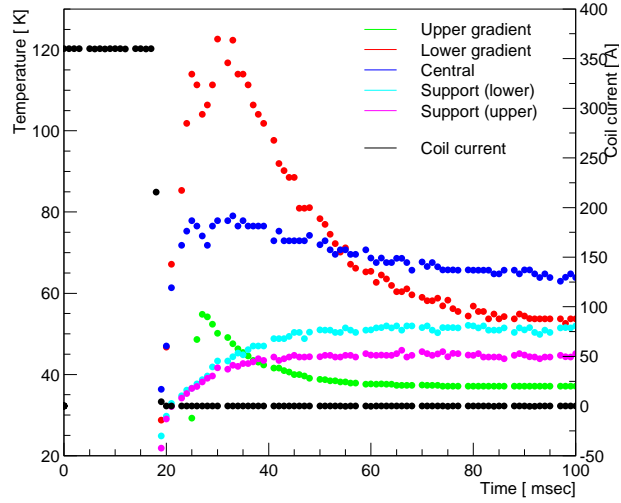


Figure 17: The temperature change of the coils and support structure when the quench occurred in the excitation #11.

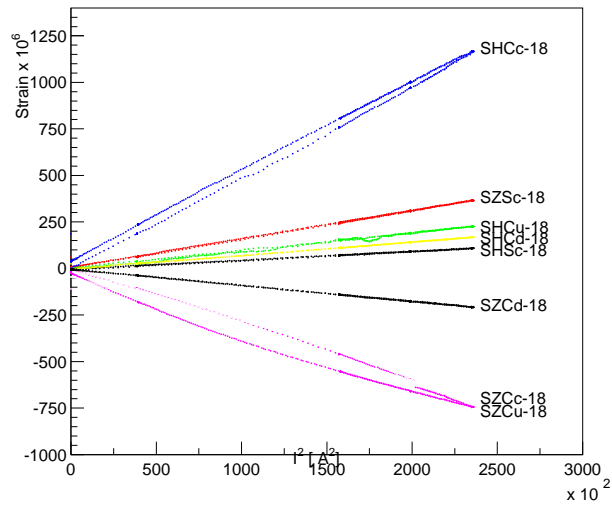


Figure 18: Change of the strain during the excitation #12.



Figure 19: The winding of the end coil where a block winding technique is employed.

## 4 Drift Chambers (DC)

On delivery of 25 new designed preamplifier chips, we were able to start our programme of tests with the two recently built chambers [1] : the charge division test chamber(CDTC) and the assembly of 4 double cathode chambers (A4DC). In parallel, we also started a systematic study of the method of mounting the cathodes, using the prototypes of the cathode hood and the middle cathodes frame (Figure 20).

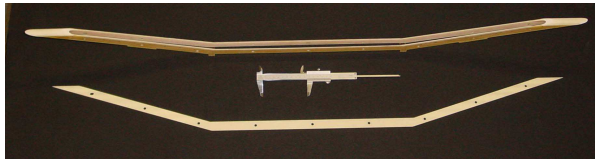


Figure 20: 1:1 Prototype of the cathode hood and the central cathode frame. The callipers define a 10 cm distance.

### 4.1 Preamplifiers and Prints

Both types of test chambers, constructed using the same print were equipped with 3 preamplifiers boards. We systematically measured the cross talk between 2 adjacent channels (wire, print and preamplifier).It was always less than 1 %. We also confirmed, that in this environment, the electronics (200-300 MHz) could be made to work in a stable way without great difficulty.

### 4.2 Double Cathode Test Chamber

We are currently working on a set-up (A4DC) that can be transported rapidly from the laboratory ( $\beta$ -particles from a  $\text{Sr}^{90}$  source, fast cosmic ray particles ) to the experimental hall ( beam particles in a 1 Tesla magnetic field). The first results correlating data from the different elements of the set-up will be taken in January 2003. Before that successive tests to externally seal and make the chambers gas-tight with a glue (THREE BONDS 1350) were performed, thus allowing a final detailed design of the chambers, based on this simple and inexpensive technique, to be realized.

### 4.3 Charge Division Test Chamber

Interesting data were taken with this 1-meter long, simply constructed chamber. Figure 21 compares the pulse shape from either end of the middle anode wire for 3 positions of a  $\text{Sr}^{90}$  source.

It can clearly be seen that the preamplifiers are fast enough to separate the individual electron clusters of the particle track. The measured start times reflect the difference in transit times of the signals along the wire to a precision better than 1 ns, proving that the contribution of the electronic and signal transport uncertainties to the drift time measurement are smaller than 1 ns.

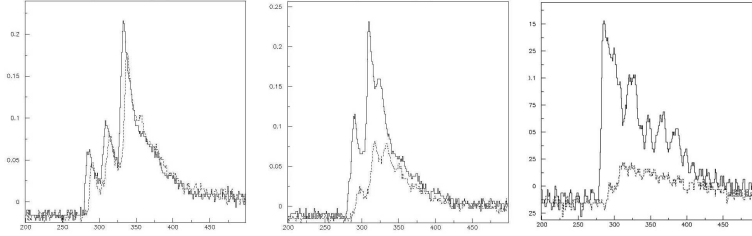


Figure 21: Charge division test chamber. Preamplifier signals at both outputs of the middle anode (time in ns). The 3 pictures corresponds to 3 positions of the  $\text{Sr}^{90}$  source: 47 cm, 71 cm and 94 cm.

Contributions such as the length of the delta electron tracks, multiple scattering, and influence of the magnetic field can only be measured accurately by the double cathode test setup (A4DC). The right/left asymmetry in the pulse shape integrals (over 200 ns) were calculated by subtracting a pedestal (flat or sinusoidal in shape as in the third picture) defined in a 200 ns region prior to the start of the signal. Figure 22 shows 5 distributions obtained at 5 equidistant positions of the  $\text{Sr}^{90}$  source, along the test wire.

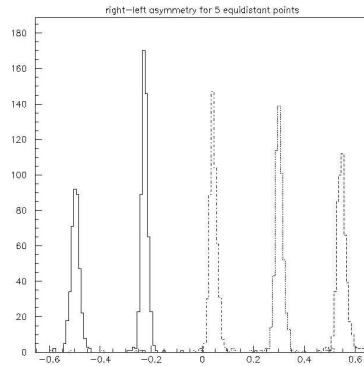


Figure 22: Sensitivity of the charge division technique with a 1-meter long steel anode wire.

For a high voltage value of 1900 V, in a Helium-Ethane gas mixture (50%-50% by volume) and without cuts on the events, the resolution obtained for the charge division method is  $\sigma = 1.5$  cm. The double cathode chamber, constructed as the final chamber works stably at 2300 V. At this higher voltage the signal-to-noise ratio is increased by a factor 4. As expected, the resolution obtained with the 1200  $\Omega/\text{m}$  steel wire is roughly 3.3 times better than the one obtained with the 330  $\Omega/\text{m}$  tungsten wire. We also confirmed that the 1.6 times larger asymmetry, obtained with a preamplifier input impedance of 50  $\Omega$  does not compensate for the factor 4.6 loss in the signal-to-noise ratio.

## 4.4 Software Development

We have started to develop the software to optimize the settings and to fully benefit from the Flash ADC technique. These tools will help us to understand and solve problems associated for example with:

- a) influence of the residual signal reflexions on the resolution (pulse shape analysis )
- b) dynamic range of signal integrals and pulse saturation (do not take in to account regions where one pulse saturates)
- c) periodic noise ( 27 MHz from the PSI HF pager system )
- d) optimization of preamplifier bandwidth and Flash ADC data sampling frequency.

## 5 Photon Detector

R&D works on the photon detector have been performed using the large prototype. The detector response has been investigated using cosmic rays, alpha sources, and 60 MeV electron beam. Preparations for the next gamma beam test which is scheduled to be carried out in the middle of February 2003 is in progress. In this section we report the progress after the last review meeting and the current status of our studies on the photon detector.

### 5.1 Large Prototype

#### 5.1.1 Cosmic Ray Test

As described in the previous report [1], it is found that remaining water in the chamber can absorb xenon scintillation light, resulting in poor light yield observed by the photomultipliers (PMTs). For reducing water contamination and increasing the light absorption length in the liquid we substituted Teflon parts with acrylic ones used in the PMT holder. The effect was verified by comparing the detector response to cosmic rays and alpha particles with Monte Carlo simulation as was done previously. In this new setup just after liquefaction the light yield for cosmic ray and alpha source events was equivalent to that after 700 hours purification in the previous setup. Together with liquefaction, gas-phase purification was performed again and the light yield for cosmic ray and alpha events was monitored periodically. It was proved that 200 hours gas-phase purification after liquefaction is enough to achieve considerably long absorption length ( $\lambda_A \geq 1\text{m}$ ) in the current setup while we had to continue purification process for more than 900 hours in the previous setup. For improving the purification speed and quality we are investigating a liquid-phase purification of xenon, as will be described in a later section.

#### 5.1.2 Electron Beam Test

Prior to a planned gamma beam test, the large prototype response to electrons has been investigated by injecting 60 MeV electrons in the center of the detector. The main purpose of the test was to evaluate the time resolution of the xenon detector using electrons. In the case of an incident gamma is not straightforward how to determine the timing of the incoming photon, but for electrons that can be easily tagged by using a plastic scintillator and PMTs. Needless to say for arrival time measurement of gamma events it is quite important to determine the depth of the first interaction point in xenon, whose uncertainty enters in the resolution of time measurement. Thus in this test the time resolution of the detector is studied only for events where the first interaction occurs just at the face of liquid xenon.

Electrons were provided from an electron storage ring at the Institute for Chemical Research, Kyoto University, Japan. The storage ring (Kaken Storage Ring, KSR) has a race track shape as shown in Figure 23 and electrons up to 60MeV can be extracted in DC mode through a septum magnet. The energy spread of electrons in KSR is less than 0.2% and the beam spot size just after extraction is 2mm in diameter<sup>3</sup>. Typical electron rate to the detector ranges

---

<sup>3</sup>This is due to the multiple scattering on the foil located at the exit of the beam line.

from 100 Hz to 10 kHz depending on the storage current in KSR. In order to

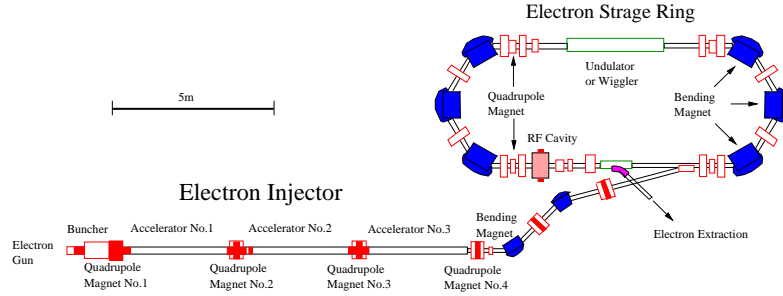


Figure 23: Layout of the electron linac and KSR.

trigger beam events and determine the start time for the TDCs, two plastic-scintillation counters of 2mm thickness each with high-speed PMTs were placed in front of the large prototype.

Data acquisition was performed in the first week of December 2002 after liquefaction and gas-phase purification for about 200 hours. Calibration of PMTs was done during data acquisition as described in the previous report [1]. Data analysis is in progress. Preliminary results are reported in the following.

Figure 24 shows a spectrum of the total number of observed photoelectrons (pe) for 60 MeV electrons extracted from KSR. Because electrons lose energy in the material placed in front of liquid xenon (the plastic scintillators, metal honeycomb window, and PMT holders), the peak corresponds to an energy deposit in liquid xenon lower than 60MeV, which is calculated to be approximately 40 MeV from Monte Carlo simulation.

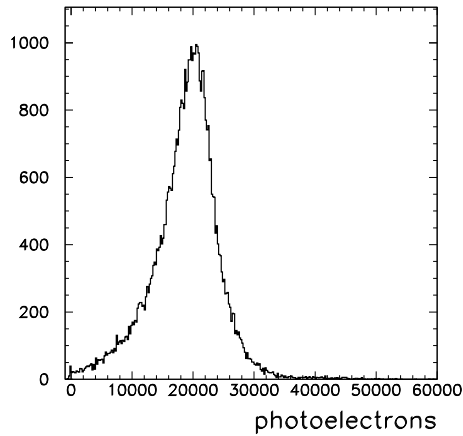


Figure 24: Distribution of total number of observed pe for 60 MeV electron incident to the setup.

For demonstrating the time measurement performance, we selected events in which the deposited energy was greater than approximately 40 MeV ( $> 20000$  pe). The detector PMTs were then divided in two groups, left and right, and the

difference of arrival time between two groups was calculated after ADC slewing correction for each PMT. A typical distribution is shown in Figure 25 with a Gaussian fit superimposed. In this analysis 87 psec time resolution (sigma) is obtained.

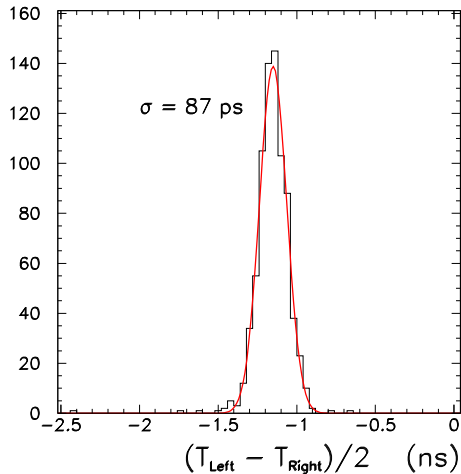


Figure 25: Distribution of measured time difference between the left and right groups of PMTs,  $T_{\text{left}}-T_{\text{right}}$ .

### 5.1.3 Gamma Beam Test

A gamma beam test scheduled in the second half of this year has been postponed due to an accelerator trouble at TERAS. The trouble is now fixed and the procedure of starting the accelerator is in progress. The test of the large prototype at TERAS is planned in the middle of February 2003.

In addition to the gamma beam test at TERAS we are investigating other methods for studying the detector performance using gamma rays above 5 MeV. One of them is to use gammas emitted from excited nuclei such as  $^{12}\text{C}$  and/or  $^8\text{Be}$ . The excited nuclei can be formed through the reactions shown in Table 4. These reactions have been used for studying resolutions of various kinds of de-

Reaction	Gamma Energy
$^9\text{Be}(^3\text{He}, \gamma)^{12}\text{C}$	$E_\gamma=31.16$ MeV
$^{11}\text{B}(p, \gamma)^{12}\text{C}$	$E_\gamma=22.38$ MeV, 17.94 MeV
$^7\text{Li}(p, \gamma)^8\text{Be}$	$E_\gamma=17.4$ MeV

Table 4: Reactions that form excited nuclei and gamma energy.

tectors like NaI crystal in the energy region below 30 MeV (see for example [7] ). The energy spread of the gammas from excited nuclei is small enough compared to the detector resolution so that we can simply evaluate the resolution from the width of the obtained gamma spectra. We are presently investigating the feasibility of such tests.

## 5.2 Photomultiplier Development

After a successful test of the first sample of the Aluminum-grid PMT, more samples of the PMT were delivered. An identical test has been repeated for each PMT to confirm that production of the PMT can be done with equivalent quality to the previous model. We are investigating carefully now the amplification gain and stability of the new model using the same setup. We have not yet encountered any serious problems up to now. The test will continue until PMT mass production.

## 5.3 Liquid Phase Purification

We started to consider the next step of xenon purification after it was pointed out in the last review meeting that we would be able to extend the absorption length more effectively by employing liquid phase purification. The key component of the purification system is a pump. The pump is required to be able to circulate low temperature fluid in a very clean condition. We are investigating the most appropriate fluid pump from view points of flow rate, heat generation, and maintenance period. The design point operating conditions of a candidate pump are listed in Table 5. Contaminant in xenon is removed by passing liquid xenon through a cell filled with molecular sieves which can capture molecules whose diameters are less than 3Å.

Fluid	Liquid Nitrogen
Inlet Pressure (maximum)	6.3 bar
Inlet Temperature	70-90K
Flow Rate	240 liter/hr
Differential Pressure	1.2 bar
Approximate Operating Speed	4500 RPM

Table 5: BNCP-50-000 design point operating conditions. [9]

Conceptual design of the liquid-phase purification system has been already started. Engineering design of the system including a test chamber where water contamination level is monitored will be started early in the year of 2003.

## 5.4 Measurement of the reflective index of liquid xenon

There is a group in Japan who plans to measure the reflective index of liquid xenon using a new method. The principle of the measurement is very simple. Liquid xenon is filled in a prism-shape glass vessel and UV-light is fed to the prism through a monochromator. The bending angle is measured with a CCD, and thus the reflective index of xenon is directly evaluated for its scintillation light wave length region. Reliable information on the reflective index is quite important because we can estimate the Rayleigh scattering length from that value as shown in [8] and also because we can estimate the reflection effect on the PMT window more precisely for the simulation. They plan to finish the measurement with a target accuracy on the reflective index of about  $\delta n=0.01$  in a few months. The result will be presented in the next Japanese physics society meeting in March 2003. Our group intend to keep a close relation with them,

and soon after their result is published, the value will be introduced into our simulation.

## 6 Electronics and DAQ

### 6.1 Slow Control System

The new slow control system "MSCB", which has been described in [1], has been refined and successfully deployed for the control of the large prototype liquid xenon detector. The so-called "rack-mounted" version of the MSCB system has been used with several cards to measure temperatures, pressures, gas flows, and LXe levels in the large prototype. Based on these values, heaters and LN2 flow have been controlled for stable operation using PID regulation loops. The control application has been written with the LabView package, utilizing the underlying MSCB hardware through newly developed device drivers. The system has been operated stably for several weeks without failure. Nevertheless, the control system for the final detector will be designed with at least two redundant subsystems. Following figure shows the control screen in the xenon circulation phase.

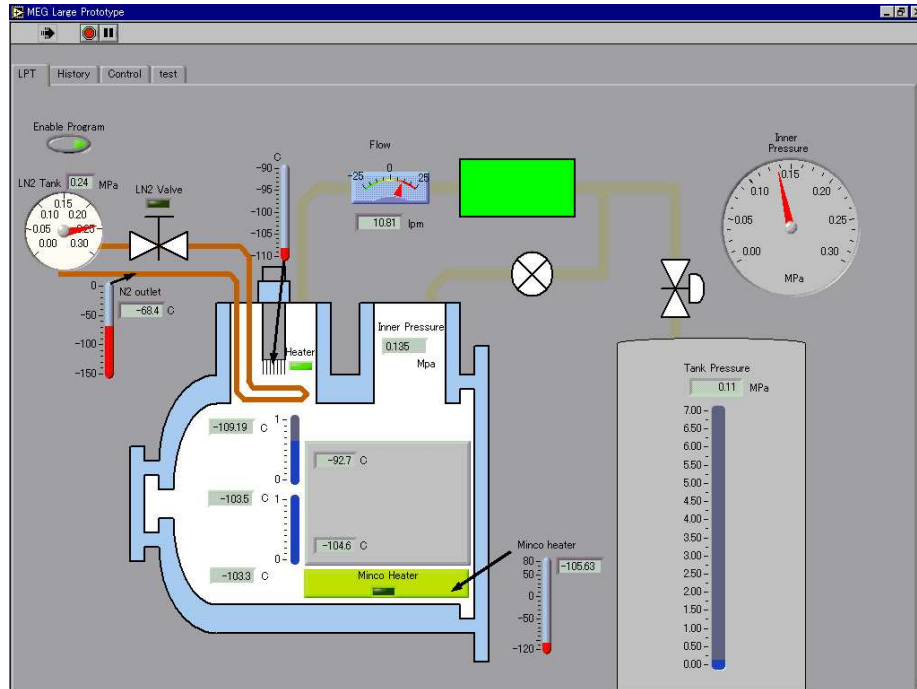


Figure 26: Control screen of the circulation phase of the large prototype. The vessel is filled with LXe, which temperature is controlled through the vessel pressure and a small heater at the refrigerator cold head.

The success of this system makes it an attractive option for other experiments. It is already used in three other PSI experiments, including the UCN-EDM experiment. More information can be found on the MSCB web site [10].

## 6.2 The DRS chip

The Domino Ring Sampler (DRS) chip is an application specific IC (ASIC) to perform waveform digitizing for all PMT channels in our experiment. This is achieved by a switched capacitor technology, which is driven by a freely running "domino" wave at a speed of 2 GHz. After a trigger occurred, the domino wave is stopped and the capacitors are read out with a commercial flash ADC at a speed of 40 MHz.

The first prototype has been submitted for manufacturing in spring 2002, as has been returned to PSI just recently. This prototype only contains a single channel with 768 cells due to space restrictions for prototype runs. First tests have shown that the chip is fully functional. The domino wave, once started, runs stably at speeds from 750MHz to 2.4GHz and depending on an external control voltage. Following figure shows an oscilloscope picture of the domino wave running at 2.4GHz.

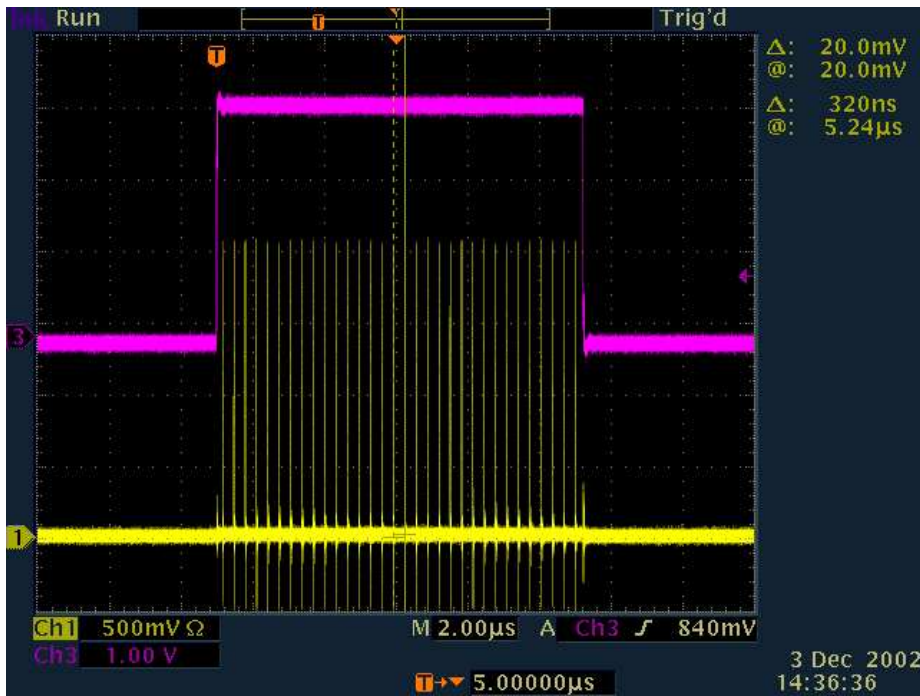


Figure 27: Oscilloscope picture of the domino wave. The upper channel shows the domino enable signal, the lower channel shows the domino pulse tapped at the middle of the chain at cell 384. The domino wave period of 340 ns corresponds to a sampling speed of  $f = \frac{1}{320ns/768} = 2.4GHz$ .

The sampling speed shows some dependence from power supply voltage and temperature, but this will be compensated by an external control logic. The domino wave will be locked to an external quartz-stabilized frequency via a digital-locked-loop (DLL) circuitry, which controls the analog domino speed voltage. A preliminary jitter measurement was performed which showed that the cell-to-cell timing inaccuracy is well below 40ps, so the chip can be used to

replace high resolution TDCs.

The readout part of the chip which consists of a dynamic shift register was successfully operated at the nominal speed of 40 MHz. First waveforms will be digitized in the following weeks, which will be reported on in the next user's meeting. Upon completion of these measurements, the final chip will be designed in early 2003.

While the MEG experiment will read out all PMTs with the DRS chip at speeds of 1-2GHz, it has been stated that the drift chamber will be digitized with our trigger boards at 100 MHz. Recent studies have shown that a higher digitizing speed for the drift chamber would be beneficial. It has been concluded that the DRS chip can be slowed down to 200 MHz with a minor design change, thus making it well suited for the drift chamber readout. Since each chip will contain eight channels, this solution is even cheaper than reading each channel with a separate 100 MHz flash ADC. Therefore we plan to use the DRS chip for all our signal channels in the MEG experiment, making the DAQ very simple with only amplifiers and one type of waveform digitizing board.

## References

- [1] MEG progress report, June 2002, <http://meg.psi.ch/docs/progress/-jun2002/report.ps.gz>
- [2] "The MEG experiment: search for the  $\mu \rightarrow e\gamma$  decay at PSI", September 2002, [http://meg.psi.ch/docs/prop\\_infn/nproposal.ps.gz](http://meg.psi.ch/docs/prop_infn/nproposal.ps.gz)
- [3] A. Baldini et al., MEG-TN018, January 2001, <http://meg.psi.ch/docs/-tnote/tn018.ps>
- [4] "Report on the Progress for the  $\mu \rightarrow e\gamma$  Experiment at PSI", Progress Report Jan. 2002.
- [5] PSI Proposal R-99.05.1, " Search for  $\mu \rightarrow e\gamma$  down to  $10^{-14}$  branching ratio", May 1999.
- [6] W. Ootani et al., MEG-TN015, June 2002. <http://meg.psi.ch/docs/-tnote/tn015.ps>
- [7] A. M. Sandorfi and M. T. Collins, Nucl. Instr. and Meth **222** (1984) 479-495.
- [8] G. M. Seidel, R. E. Lanou and W. Yao, "Rayleigh scattering in rare-gas liquids" hep-ex/0111054
- [9] Barber-Nichols, 6325 West 55th Ave. Arvada, Colorado 80002, <http://www.barber-nichols.com/>.
- [10] MSCB home page, <http://midas.psi.ch/mscb>